ACS OMEGA

http://pubs.acs.org/journal/acsodf

Article

Three-Dimensional Porous Network Electrodes with $Cu(OH)_2$ Nanosheet/Ni_3S_2 Nanowire 2D/1D Heterostructures for Remarkably Cycle-Stable Supercapacitors

Jiansen Wang,[#] Libing Hu,[#] Xiaoya Zhou, Sheng Zhang, Qingshan Qiao, Lei Xu,* and Shaochun Tang*

Cite This: *ACS Omega* 2021, 6, 34276−34285

Read Online

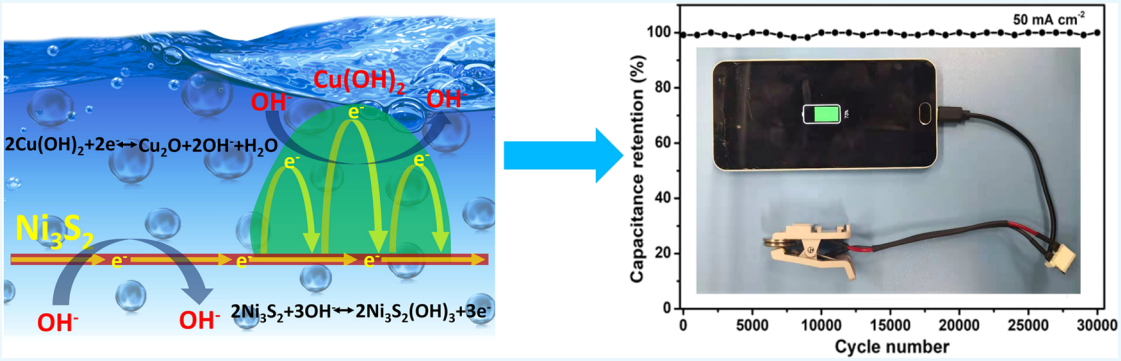

ABSTRACT: Developing advanced electrode materials with highly improved charge and mass transfer is critical to obtain high specific capacities and long-term cycle life for energy storage. Herein, three-dimensionally (3D) porous network electrodes with $Cu(OH)_2$ nanosheets/Ni_3S_2 nanowire 2D/1D heterostructures are rationally fabricated. Different from traditional surface deposition, the 1D/2D heterostructure network is obtained by *in situ* hydrothermal chemical etching of the surface layer of nickel foam (NF) ligaments. The $Cu(OH)_2/Ni_3S_2$@NF electrode delivers a high specific capacity (1855 F g^{-1} at 2 mA cm^{-2}) together with a remarkable stability. The capacity retention of the electrode is over 110% after 35,000 charge/discharge cycles at 20 mA cm^{-2}. The improved performance is attributed to the enhanced electron transfer between 1D Ni_3S_2 and 2D $Cu(OH)_2$, highly accessible sites of 3D network for electrolyte ions, and strong mechanical bonding and good electrical connection between $Cu(OH)_2/Ni_3S_2$ active materials and the conductive NF. Especially, the unique 1D/2D heterostructure alleviates structural pulverization during the ion insertion/desertion process. A symmetric device applying the $Cu(OH)_2/Ni_3S_2$@NF electrode exhibits a remarkable cycling stability with the capacitance retention maintaining over 98% after 30,000 cycles at 50 mA cm^{-2}. Therefore, the outstanding performance promises the architectural 1D/2D heterostructure to offer potential applications in future electrochemical energy storage.

1. INTRODUCTION

With the ever-increasing growth of portable devices, the increasing demand for efficient energy supply for electronic devices is becoming more and more impending.[1−4] Advanced energy storage systems with expectative battery performance are highly required. To this regard, supercapacitors (SCs) are considered as a competitive one due to their inherent advantages of low cost, high safety, fast charge/discharge, and long usage life.[5−8] In spite of this, the relatively low energy density (≤10 Wh kg^{-1}) together with the unsatisfying long-life cycling stability at too high discharging rates is the main problems with SCs, which severely inhibits their commercial application.[9−11] According to the charge storage mechanisms, electrode materials of SCs are divided into electric double-layer capacitors (EDLCs) and pseudocapacitors.[6,12−15] The latter stores energy by the adsorption of near-surface ions, and the fast reversible Faradic reactions lead to additional contribution taking place on the electrode materials' surface. This makes the latter have much higher electrochemical capacities and energy densities than the EDLCs.[16−19] Therefore, developing new pseudocapacitive electrode materials is highly expected to break the ceiling of performance limit of SCs.

Among the pseudocapacitive materials available, transitional metal sulfides exhibit more enhanced electrical conductivity than their oxide counterparts and have been regarded as one

Received: July 5, 2021
Accepted: August 20, 2021
Published: December 10, 2021

https://doi.org/10.1021/acsomega.1c03507
ACS Omega 2021, 6, 34276−34285

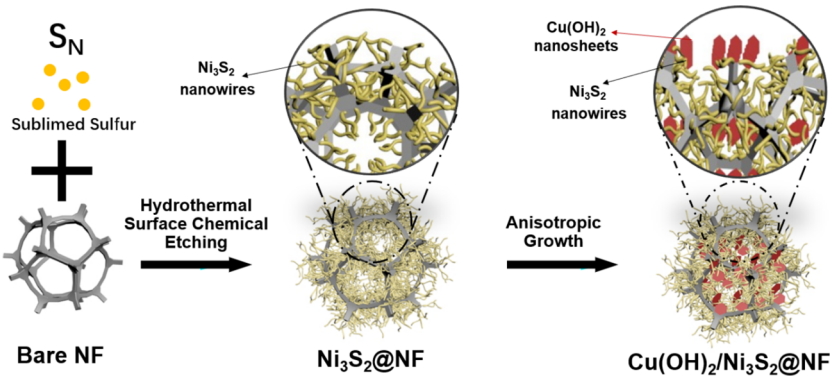

Figure 1. Schematic illustration of the synthetic route of the heterostructures constructed by 1D Ni_3S_2 nanowires and 2D $Cu(OH)_2$ nanosheets.

kind of the most potential candidates for SCs.[20−22] Nickel sulfides such as Ni_3S_2 has attracted particular attention for high-performance SCs due to its high theoretical specific capacity (2412 F g^{-1}), high intrinsic electrical conductivity, cheap and rich resources, fluent charge transfer, and environmental benignancy.[23−26] In the past decades, Ni_3S_2 nanostructures with various nanoshapes (such as particles, flakes, and so on) were prepared for SCs.[27−29] Compared with these various shapes, one-dimensional (1D) nanorods/nanowires/nanotubes with a large length-to-diameter ratio show lower electrode resistances and better durability because the high anisotropy strongly enhances the electrical conductivity and largely exposed surfaces provide sufficient contacts with electrolyte ions.[30] Nevertheless, they are easy to form into aggregations because of an existence of strong van der Waals forces, which lowers the active area for ions to be fully accessible. Specific capacitances of the reported Ni_3S_2 electrode materials are far lower than their theoretical value and suffer from the limitations of short cycle life. Therefore, it is still a great challenge to completely combine these advantages of Ni_3S_2 to boost its inherent potential for energy storage.

Recent achievements have confirmed that heterostructures composed of different materials can provide significantly enhanced electrochemical performances by combining the advantages of different components because the electron/ion migration paths can be optimized through construction of heterostructures, and sufficient exposure of active sites can be offered.[31−33] In 1D/2D heterostructures, 1D materials can supply an efficient path for the electron transport; meanwhile, 2D nanosheets can guarantee a larger surface area to offer sufficient exposure of active sites.[34−38] Therefore, developing heterostructures by combining 1D Ni_3S_2 with suitable 2D pseudocapacitive materials is able to improve electrochemical performance. Enormous efforts have been devoted to constructing composite electrode systems involving active nanosized Ni_3S_2.[39−43] For instance, a hierarchical $NiCo_2O_4$ nanowire@Ni_3S_2 nanosheet takes good advantage of 1D and 2D merits to obtain a high performance for SCs.[44] Copper-based hydroxides are regarded as the most promising pseudocapacitive materials contributing to their chemical stability, low cost, easy preparation, and environmental benignancy.[45−47] For example, 1D $Cu(OH)_2$ nanowires on carbon cloth as an electrode material were reported to show a high areal specific capacitance for SCs.[48] Inspired by this, 2D $Cu(OH)_2$ nanostructures are an ideal candidate to combine with 1D Ni_3S_2 to form an advanced electrode with heterostructures that also make up for the poor electrical conductivity of $Cu(OH)_2$ itself. Based on these, it is thus expected that the resulting electrode will deliver a significant improvement of the SCs' performance. To the best of our knowledge, heterostructures consisting of 1D Ni_3S_2 and 2D $Cu(OH)_2$ for SCs have not been reported yet.

Inspired by the abovementioned characteristics, we herein developed novel electrodes consisting of 2D $Cu(OH)_2$ nanosheet-covered 1D Ni_3S_2 nanowire networks on nickel foam (NF) by applying a two-step hydrothermal process. First, 1D Ni_3S_2 nanowires formed on the ligaments of NF via a surface chemical etching of NF under a hydrothermal environment, and then ultrathin 2D $Cu(OH)_2$ nanosheets were generated on the preformed Ni_3S_2 nanowires. The unique 1D/2D heterostructure provides a great contact area with electrolyte ions and active sites while alleviating structural pulverization during the process of ion insertion and desertion. The obtained $Cu(OH)_2/Ni_3S_2$ electrode displayed high specific capacitances and a long-term cycle reversibility. Furthermore, an assembled symmetric solid-state device showed a remarkable recycling stability with the capacitance retention maintaining over 98% after 30,000 charge and discharge cycles at 50 mA cm^{-2}. In addition, the practical application was demonstrated by powering a mobile phone using two connected coin-type cells.

2. RESULTS AND DISCUSSION

The synthetic process of the 1D/2D heterostructure constructed by 1D Ni_3S_2 nanowires and 2D $Cu(OH)_2$ nanosheets includes two-step hydrothermal processes, which is schematically shown in Figure 1. First, 1D Ni_3S_2 nanowires grow on the ligaments of bare nickel foam by direct *in situ* sulfurization etching of the surface of NF's ligaments. During the process, at 160 °C under a hydrothermal environment, the chemical reaction between the sublimed sulfur (S_N) with ethylenediamine leads to H_2S. Then, the generated H_2S reacts with NF to result in the generation of Ni_3S_2. One-dimensional Ni_3S_2 nanowires successfully form on the ligaments of 3D porous NF due to an anisotropic growth during the *in situ* chemical etching and growth process. The possible reaction equations are as follows:[49]

$$S_N + 2\,NH_2CH_2CH_2NH_2 \rightarrow NH_2CH_2CH_2NH - S_{N-1} - HNCH_2CH_2\,NH_2 + H_2S \quad (1)$$

$$2H_2S + 3\,Ni \rightarrow Ni_3S_2 + 2\,H_2 \quad (2)$$

https://doi.org/10.1021/acsomega.1c03507
ACS Omega 2021, 6, 34276−34285

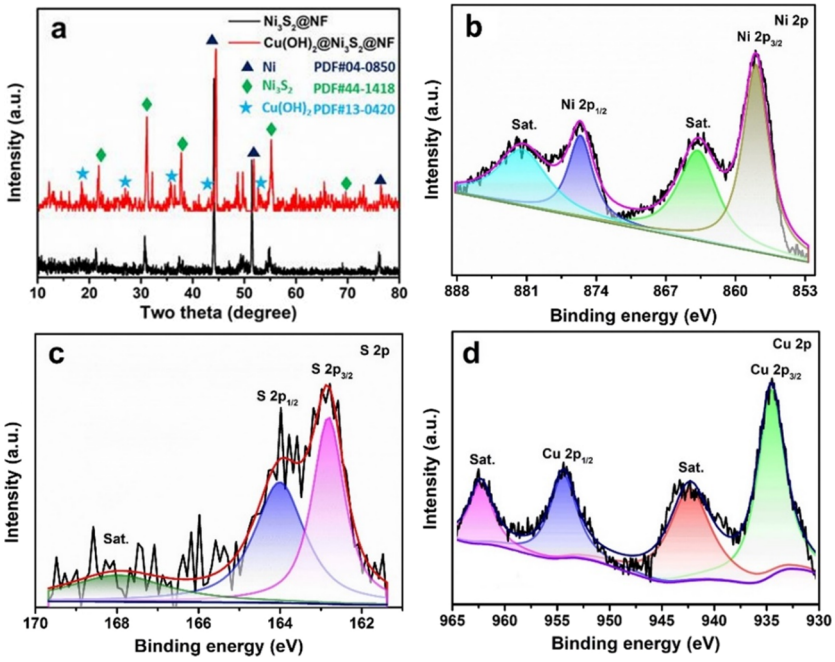

Figure 2. (a) XRD patterns of $Cu(OH)_2/Ni_3S_2$@NF and Ni_3S_2@NF. High-resolution XPS spectra of (b) Ni 2p, (c) S 2p, and (d) Cu 2p for $Cu(OH)_2/Ni_3S_2$@NF.

In the subsequent synthetic step, $Cu(OH)_2$ nucleates on the surfaces of individual Ni_3S_2 nanowires after Cu^{2+} ions react with OH^- ions in the alkaline solution. The growth rate of $Cu(OH)_2$ mainly depends on the concentration of Cu^{2+} ions, and the resulting morphology of grown $Cu(OH)_2$ nanostructures can be controllable. When the typical Cu^{2+} concentration is 0.125 M, the $Cu(OH)_2$ nuclei grow up in an anisotropic growth way, and standing 2D $Cu(OH)_2$ nanosheets from surrounding each Ni_3S_2 nanowire. Simultaneously, the 1D/2D heterostructures are successfully constructed by the newly formed 2D $Cu(OH)_2$ nanosheets covering the 1D Ni_3S_2 nanowires.

The advantages of 1D/2D heterostructure network structures on 3D porous NF for SCs are suggested as follows. Since Ni_3S_2 is of high conductivity, the 3D network of Ni_3S_2 nanowires not only guarantees good electron transfer to $Cu(OH)_2$ nanosheets but also acts as a skeleton to avoid their aggravation. Moreover, the synergistic effect between the grown 2D $Cu(OH)_2$ nanosheets and 1D Ni_3S_2 nanowires promotes efficient reversible Faradic reactions. In addition, the 1D/2D heterostructures on the NF with lightweight, high porosity, and excellent electrical conductivity ensure large surface areas to offer sufficient exposed surface active sites. Therefore, the NF-supported $Cu(OH)_2/Ni_3S_2$ networks are able to deliver high capacitance and long-term cycling stability even at high discharging rates.

Figure 2a shows the XRD pattern of $Cu(OH)_2/Ni_3S_2$@NF (the red one), and the XRD pattern of Ni_3S_2@NF (the black one) is also presented for comparison. Obviously, three sharp diffraction peaks at 43.9, 51.3 and 75.9° correspond to (111), (200), and (220) planes of NF (JCPDS PDF #04-0850). In addition, other five apparent peaks correspond to Ni_3S_2 with high crystalline phase (JCPDS PDF #44-1418). It should be noted that the other five diffraction peaks indexing to $Cu(OH)_2$ (JCPDS PDF #13-0240) are also clearly observable for $Cu(OH)_2/Ni_3S_2$@NF but not for Ni_3S_2@NF, which confirms that $Cu(OH)_2$ successfully forms in the obtained sample after Cu^{2+} ions react with OH^- ions during the second step hydrothermal synthesis in an alkaline solution.

Figure 2b−d show XPS spectra of the typical $Cu(OH)_2/Ni_3S_2$@NF, which further check the main elements of Ni, S, and Cu and their chemical states. The high-resolution Ni 2p spectrum (Figure 2b) is deconvoluted into two dominant peaks for Ni $2p_{3/2}$ (873.1 eV) and Ni $2p_{1/2}$ (855.7 eV) with two satellite signals (879.5 and 861.4 eV). These match with Ni^{2+} very well. For the S 2p spectrum (Figure 2c), two peaks contributing to S $2p_{3/2}$ and S $2p_{1/2}$ components of S^{2-} are found at 163.3 and 162.1 eV, respectively. Another weak peak at 168.0 eV is the satellite peak. These peaks coordinate with S in the Ni_3S_2 phase, which confirm that Ni_3S_2 is kept well in the resulting product after the hydrothermal growth of $Cu(OH)_2$. Furthermore, the high-resolution XPS Cu 2p spectrum in Figure 2d displays a peak for Cu $2p_{3/2}$ (934.5 eV) and a satellite peak (at 942.3 eV), suggesting that the valence state of Cu in the product is +2, which is consistent with $Cu(OH)_2$.[50] Therefore, the XPS analysis also confirms that the resulting product consists of Ni_3S_2 and $Cu(OH)_2$, which agrees with the XRD results very well.

Figure 3a,c displays the low-magnification SEM images for the Ni_3S_2@NF and $Cu(OH)_2/Ni_3S_2$@NF electrodes. It is observed that the three-dimensional porous structure of bare NF is maintained well in the samples. Obviously, more folds are present on the NF skeleton in $Cu(OH)_2/Ni_3S_2$@NF than those on Ni_3S_2@NF. From high-magnification SEM images (Figure 3b), a uniform coverage of Ni_3S_2 nanowires can be seen on the ligaments of the NF surface. After growth of $Cu(OH)_2$, the 3D network of Ni_3S_2 nanowires (Figure 3d) were kept well; meanwhile, a large number of 2D nanosheets are distributed among the nanowires to construct 1D/2D heterostructures.

The morphology and nanostructure are further observed by using TEM. As it can be observed in Figure 4a, a low-magnification TEM image exhibits that $Cu(OH)_2/Ni_3S_2$ is separated from the ligaments of NF. It consists of 1D

https://doi.org/10.1021/acsomega.1c03507
ACS Omega 2021, 6, 34276−34285

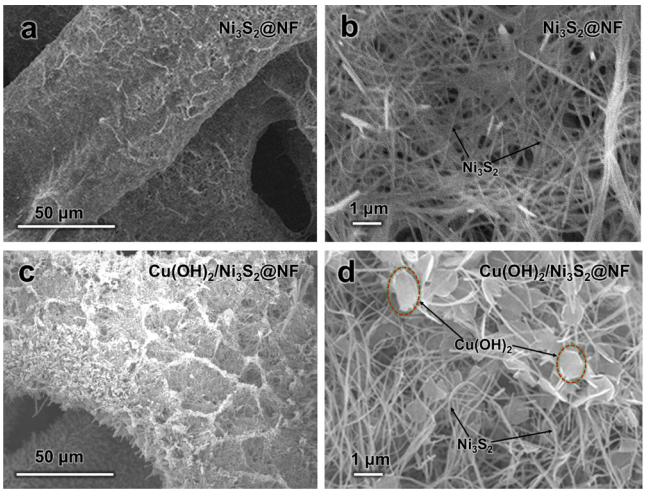

Figure 3. SEM images at different magnifications of (a, b) Ni_3S_2@NF and (c, d) $Cu(OH)_2/Ni_3S_2$@NF. The thin nanosheets in the dashed circles in (d) are $Cu(OH)_2$.

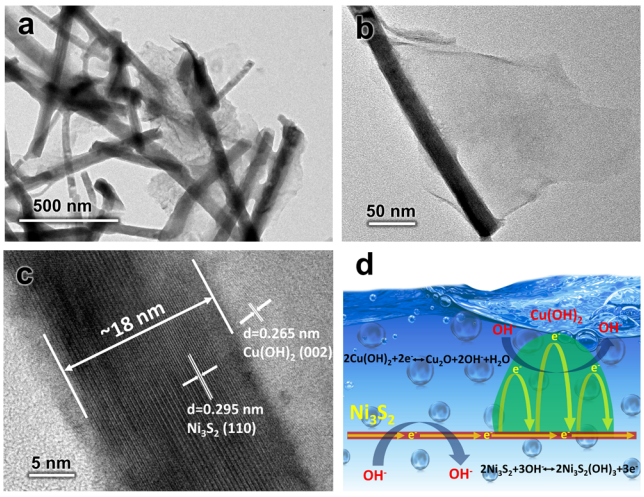

Figure 4. (a, b) TEM images for $Cu(OH)_2/Ni_3S_2$ separated from the ligaments of NF. (c) HRTEM image for $Cu(OH)_2/Ni_3S_2$. (d) Charge/discharge mechanism of the 1D/2D heterostructure for SCs in a KOH electrolyte.

nanowires and 2D nanosheets. A TEM image at a higher magnification (Figure 4b) confirms that the Ni_3S_2 nanowires have an average diameter of about 18 nm, in accordance with the SEM analysis result. On one side of the nanowire, a 2D thin nanosheet grows on it. Therefore, it is obvious that the 1D nanowires and 2D nanosheets constructed the desirable 1D/2D heterostructure. An HRTEM image (Figure 4c) exhibits a series of lattice fringes; a spacing of 0.29 nm belongs to the (110) crystallographic plane of Ni_3S_2. In the nanosheet area, the interlayer distance of lattice fringes is measured to be 0.26 nm, indexing to the (002) plane of $Cu(OH)_2$. Therefore, the combined results of the TEM and HRTEM images further confirm that the obtained heterostructures are composed of 1D Ni_3S_2 nanowires and 2D $Cu(OH)_2$ nanosheets.

As is reported, Ni_3S_2 has the ability of compatibility with electrolyte ions and high conductivity for charge transfer, and thus electrons are free to transfer in a Ni_3S_2 nanowire. When used in electrochemical energy storage, these properties of Ni_3S_2 result in reversible redox reactions of Ni^{2+}/Ni^{3+} in a 3 M KOH, and the related reaction follows the equation $Ni_3S_2 + 3OH^- \leftrightarrow Ni_3S_2(OH)_3 + 3e^-$.[44] The newly grown 2D $Cu(OH)_2$ delivers fast transportation of electrons with an assistance of the 1D Ni_3S_2 and possesses a high contacting area for OH^- ions transfer due to richness in ion-accessible active sites and exposed surfaces/edges. The related redox reactions for the active material ($Cu(OH)_2$) take place according to the following equation: $2Cu(OH)_2 + 2e^- \leftrightarrow Cu_2O + 2OH^- + H_2O$.[48] The 1D/2D heterostructures for electrochemical energy storage are shown in Figure 4d. Figure 5a shows N_2 adsorption−desorption isotherms of the two electrodes, and an obvious difference is observed. In particular, in the isotherms of the $Cu(OH)_2/Ni_3S_2$@NF electrode, the slope of the curves rises remarkably with a relative pressure above ∼0.95, which is attributed to the nanostructure change induced by the $Cu(OH)_2$ nanosheets. $Cu(OH)_2/Ni_3S_2$@NF delivers a relatively higher BET specific surface area (42.63 $m^2\ g^{-1}$) than Ni_3S_2@NF (21.76 $m^2\ g^{-1}$), which is attributed to the 3D nanowire network and 2D grown nanosheets. Their pore diameters are distributed in a range of 2−5 nm (Figure 5b), and the $Cu(OH)_2/Ni_3S_2$@NF electrode has much more pores than the Ni_3S_2@NF one.

Electrochemical examination of the obtained $Cu(OH)_2/Ni_3S_2$@NF is conducted by cyclic voltammetry (CV) measurements in an electrochemical potential window ranging from −0.2 to 0.8 V in a 3 M KOH electrolyte. Figure 6a,c shows CV curves at different scan rates for the Ni_3S_2@NF and $Cu(OH)_2/Ni_3S_2$@NF electrodes, respectively. All of the CV curves have an oxidation peak during the charge stage and a reduction peak in the discharge process. This behavior indicates that the capacities of the two electrodes are mainly from the pseudocapacitance. As shown in Figure 6a, a pair of redox

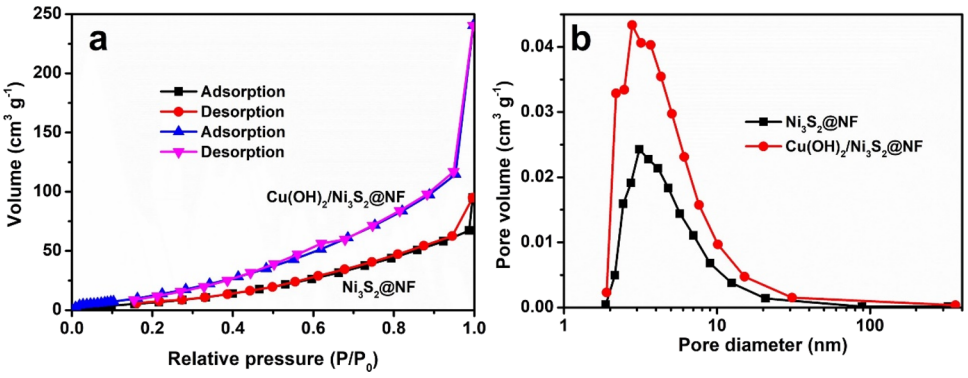

Figure 5. (a) Nitrogen adsorption/desorption isotherms and (b) corresponding pore size distribution of Ni_3S_2@NF and $Cu(OH)_2/Ni_3S_2$@NF.

https://doi.org/10.1021/acsomega.1c03507
ACS Omega 2021, 6, 34276−34285

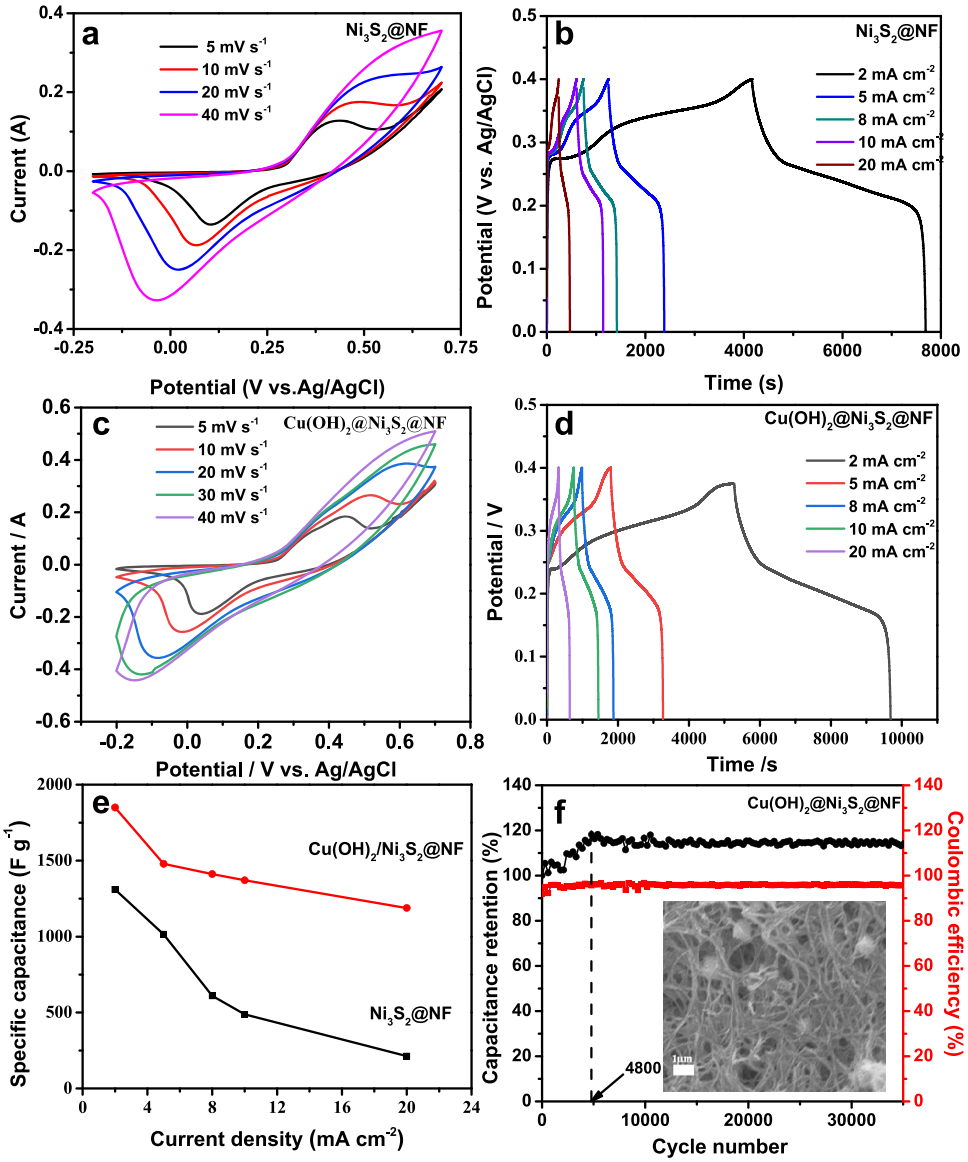

Figure 6. CV curves at different scan rates and GCD curves at different current densities of (a, b) Ni_3S_2@NF and (c, d) $Cu(OH)_2/Ni_3S_2$@NF electrodes. (e) Comparison of specific capacitances. (f) Capacitance retention and Coulombic efficiency of $Cu(OH)_2/Ni_3S_2$@NF over 35,000 cycles at 20 mA cm^{-2} in a 3 M KOH solution, with the inset showing an SEM image of the electrode after the 35,000th cycle.

peaks located at about 0.05 and 0.3 V with a scan rate of 5 mV s^{-1} belonging to the reversible Faradic redox reactions of Ni(II)/Ni(III). In the curve of $Cu(OH)_2/Ni_3S_2$@NF at the same scan rate (see Figure 6c), a pair of redox peaks appeared at about 0.05 and 0.43 V, attributed to the reversible Faradic redox reactions of Ni(II)/Ni(III) and Cu(II)/Cu(I), respectively. Compared with the curves of Ni_3S_2@NF, the reduction peak shifts more negatively and simultaneously the oxidation peak shifts more positively in the curves for $Cu(OH)_2/Ni_3S_2$@NF. This might be due to the fact that the improvement of OH^- transfer is helped by Cu^+/Cu^{2+} and Ni^{2+}/Ni^{3+}, which demonstrates the specific pseudocapacitive contributions of Ni_3S_2 and $Cu(OH)_2$ in the electrode. According to the CV results, the diffusion-controlled process dominates the electrochemical reactions, which is in accordance with the hierarchically 3D nanowire network structure and richness in 1D/2D interfaces promoting the electrolyte diffusion. The electron/ion transfer of the interfacial redox reactions has a faster kinetics for $Cu(OH)_2/Ni_3S_2$@NF. Under the same scan rate, the integrated area of CV curves for $Cu(OH)_2/Ni_3S_2$@NF is larger than that for Ni_3S_2@NF, which suggests that the former has a higher electrochemical capacity.[51] The improvement is because the thin $Cu(OH)_2$ nanosheets strongly give pseudocapacitive contribution by supplying much more much charges.

Furthermore, galvanostatic charge and discharge (GCD) of the two electrodes are performed and the obtained curves are presented in Figure 6b,d. It is observed that two obvious well-defined voltage plateaus corresponding to the Faradic redox reaction appear during the charge/discharge process, in good agreement with the redox peaks. Specific capacitances are obtained according to the discharge curve from the reported equation $C = I\Delta t/(m\Delta V)$, and the discharge times of the $Cu(OH)_2/$ Ni_3S_2@NF heterostructure are much longer than those of Ni_3S_2@NF at the same current densities. The CV and GCD results suggest that $Cu(OH)_2/Ni_3S_2$@NF has a better electrochemical performance. Specific capacitances of the Ni_3S_2@NF and $Cu(OH)_2/Ni_3S_2$@NF electrodes at various

https://doi.org/10.1021/acsomega.1c03507
ACS Omega 2021, 6, 34276−34285

current densities are presented in Figure 6e. Specific capacitances of the $Cu(OH)_2/Ni_3S_2$@NF electrode are calculated to be 1855, 1479, 1412, 1371, and 1188 F g^{-1} at 2, 5, 8, 10, and 20 A cm^{-1}, respectively. As expected, these values are much higher than those of the Ni_3S_2@NF electrode (1310, 1015.2, 610.5, 487.6, and 212.6 F g^{-1} at the corresponding current densities). In general, the large specific surface area and porous network structure can enhance the active sites and improve the electrochemical performance. As discussed in Figure 5, the higher BET value of $Cu(OH)_2/Ni_3S_2$@NF and hierarchical distribution of pores facilitate faster ion transport and assure higher rate performance. The improved electrochemical performance should be attributed to the combined advantages of the 1D/2D heterostructures of $Cu(OH)_2/Ni_3S_2$. One-dimensional Ni_3S_2 nanowires grown on the NF surface facilitate the electron transport and boost the electrical conductivity in $Cu(OH)_2/Ni_3S_2$@NF; meanwhile, 2D ultrathin $Cu(OH)_2$ nanosheets are distributed among the nanowires networks, remarkably increasing the amount of electroactive sites, which is able to efficiently accelerate the process of the ion's diffusion and diminish the diffusion distance to the interior surfaces in the electrode.

The cycling stability is also another important index for SCs. To further examine the recycling stability of the as-obtained $Cu(OH)_2/Ni_3S_2$@NF electrode, the cycling performance is performed by GCD tests in a 3 M KOH solution. With a high current density at 20 mA cm^{-2}, the specific capacitance of $Cu(OH)_2/Ni_3S_2$@NF increases by 18.2% in the initial 4800 cycles (the black curve), as shown in Figure 6f. The possible reason is that the $Cu(OH)_2/Ni_3S_2$@NF electrode is selectively etched in a 3 M KOH alkaline solution and further activated electrochemically in the initial cycling process, which is able to increase the electroactive surface area and to improve their wettability, and these changes encourage the trapped electrolyte ions to diffuse out. Although the capacitance displays slight fluctuations after the initial increase, its specific capacitance still keeps beyond 110% of the initial specific capacitance after 35,000 cycles. This is because the active material with the unique heterostructures had been absolutely contacted with the electrolyte ions after 4800 cycles, and more electrochemical active sites participated in the oxidation−reduction reaction. This is quite common in many other reported works.[52−54] Coulombic efficiency is calculated based on the reported equation $\eta = t_d / t_c \times 100\%$, in which t_c and t_d stand for the charge time and discharge time, respectively.[55] Notably, the Coulombic efficiency of $Cu(OH)_2/Ni_3S_2$@NF keeps a good stability with a value of 95.6% ± 0.5% and no drastic fluctuation can be observed during the whole cycling measurements (the red curve). This means that there is no significant reduction in the ratio of t_d to t_c during continuous charge−discharge cycles, which is mainly due to the obtained unique nanostructure. Therefore, $Cu(OH)_2/Ni_3S_2$@NF shows an excellent charge−discharge long-term electrochemical durability for energy storage. The inset of Figure 6f shows an SEM image of the electrode after continuous 35,000 cycles at a high current density of 20 mA cm^{-2}. It can be observed that the whole morphology and the intact 3D network structure are remained well after the cycling, which further demonstrates that the $Cu(OH)_2/Ni_3S_2$@NF electrode has an excellent cyclic stability.

The intrinsic difference of the interfacial redox reaction kinetics between the two electrodes is highly dependent on the internal resistances that can be analyzed by electrochemical impedance spectroscopy (EIS) measurements. Nyquist plots of the two electrodes are shown in Figure 7. The inset picture

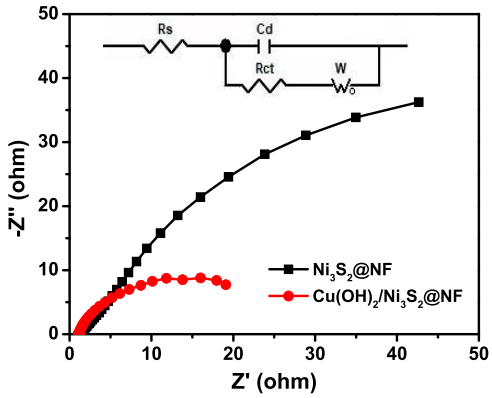

Figure 7. Nyquist plots of the Ni_3S_2@NF and $Cu(OH)_2/Ni_3S_2$@NF electrodes.

shows the proposed equivalent circuit applied to gain the electrochemical parameters, where R_s stands for the resistance of the electrolyte solution, R_{ct} denotes the Faradic charge transfer resistance, C_d represents the double-layer capacitance, and W expresses the Warburg impedance, which stands for the electrolyte diffusion. The Nyquist plots of both the electrodes display a small semicircle expressed by an almost vertical line. The $Cu(OH)_2/Ni_3S_2$@NF electrode displays an R_{ct} value of 1.08 Ω, which is smaller than the Ni_3S_2@NF electrode (R_{ct} = 1.3 Ω). The smaller internal resistance is owing to the thin $Cu(OH)_2$ nanosheets, which are well separated apart and maintained a space for the electrolyte to reach the surface of the Ni_3S_2 nanowires. $Cu(OH)_2/Ni_3S_2$@NF has much more active sites available and a faster ion/charge transport kinetics, and the redox reactions are thus increased.

A two-electrode symmetric device as a coin-type cell is fabricated by assembling two pieces of $Cu(OH)_2/Ni_3S_2$@NF (1 cm × 1 cm) with the same mass as the positive electrode and the negative electrode, respectively. A schematic configuration of the designed coin-type cell is illustrated in Figure 8a. The GCD curves of the assembled supercapacitor (ASC) examined at 3, 5, 10, 20, and 50 mA cm^{-2} are represented in Figure 8b. It can be clearly seen that all of the GCD curves at varying current densities remain in good symmetry at different cell voltages, suggesting that the device has an outstanding electrochemical reversibility. Based on the GCD curves (Figure 8c), the ASC gives a specific capacitance of 47.6, 34.6, 25.5, 18.1, and 10.4 F g^{-1} at different current densities (3, 5, 10, 20, and 50 mA cm^{-2}), respectively. More importantly, an inset digital image shows that the cell is able to deliver the current normally, which promises potential applications.

To further investigate the stable performance for the assembled coin-type cell, the cell is subjected to 30,000 cycles of full-depth charge and discharge at 50 mA cm^{-2} in a 3 M KOH electrolyte. As shown in Figure 8d, although a slight fluctuation is present in the capacitance during the long-time cycling test due to the minor temperature variation, the capacitance retention of the cell still remains more than 98% after this long-term cycling, which can be attributed to the 1D/2D heterostructures. More importantly, two of the assembled ASCs are able to power a mobile phone, as displayed by the

https://doi.org/10.1021/acsomega.1c03507
ACS Omega 2021, 6, 34276−34285

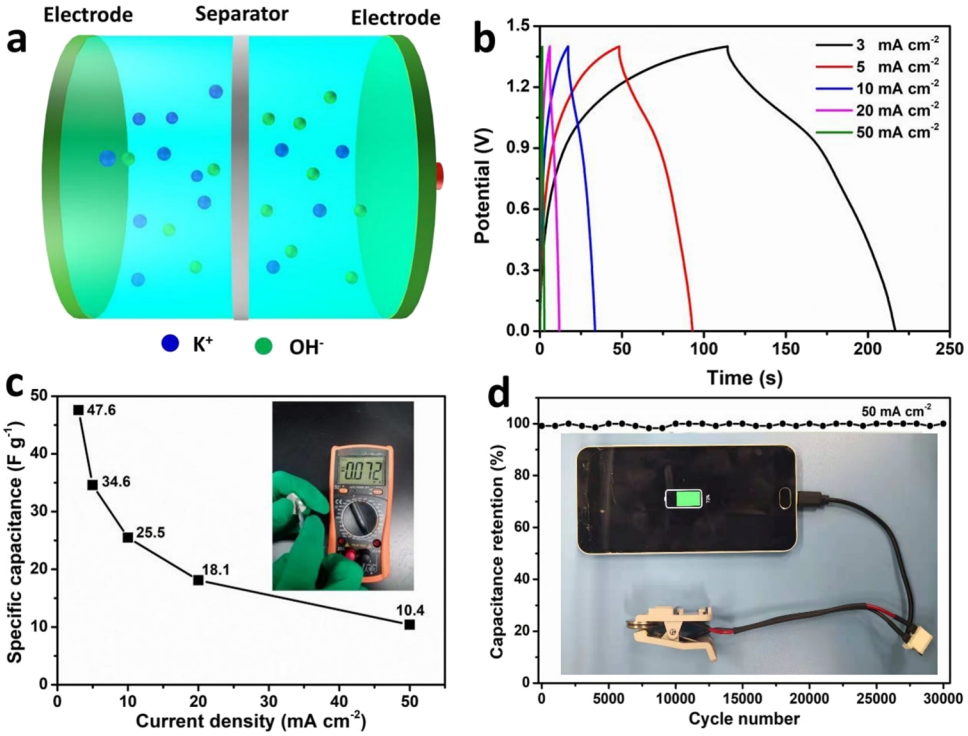

Figure 8. (a) Illustration of the configuration of a two-electrode symmetric supercapacitor as a coin-type cell. (b) GCD curves at various current densities of $Cu(OH)_2/Ni_3S_2$@NF//$Cu(OH)_2/Ni_3S_2$@NF. (c) Corresponding specific capacitances of the electrodes at different current densities and digital photos of one coin-type cell connected with a multimeter (inset). (d) Cycling test over 30,000 cycles at 50 mA cm^{-2} and two coin-type cells connected with a mobile phone (inset).

inset digital image in Figure 8d. The excellent performance opens many opportunities for miniaturized electronic devices.

3. CONCLUSIONS

In summary, we demonstrate the fabrication of 1D Ni_3S_2 nanowire/2D $Cu(OH)_2$ nanosheet heterostructures by two-step hydrothermal reactions. First, the surface layer of NF is sulfidated, leading to an *in situ* growth of 1D Ni_3S_2 nanowire networks. In the following hydrothermal process, Cu^{2+} ions react with hydroxide ions to form 2D $Cu(OH)_2$ nanosheets, which cover the 1D Ni_3S_2 nanowires to construct 1D/2D heterostructures. The $Cu(OH)_2/Ni_3S_2$@NF electrode demonstrates enhanced electrochemical performance with a superior cyclic performance of more than 110% capacity retention at 20 mA cm^{-2} over 35,000 cycles. Especially, the ASC delivers an outstanding long-life recycling stability, maintaining a capacitance retention of more than 98% at 50 mA cm^{-2} after 30,000 cycles. The improved performance for SCs is owing to the unique architecture supplying a high contacting area between the electrolyte with the active sites, alleviated structural pulverization during the process of the ion insertion and desertion, a good electrical conductivity for increased ions/charge kinetics, and a synergistic effect between 1D Ni_3S_2 nanowires and 2D $Cu(OH)_2$ nanosheets. This encouraging work provides a new path for developing heterostructures for high-rate and cycle-stable energy storage.

4. EXPERIMENTAL SECTION

4.1. Materials' Preparation. *4.1.1. Preparation of Ni_3S_2@NF.* A piece of thin NF (2 cm × 2 cm) was cleaned in a 1 M HCl solution for 10 min under ultrasonic irradiation and then was washed by using deionized water and absolute ethanol few times. Subsequently, the NF was put into a vacuum oven to be dried. Typically, 2 mmol of sublimed sulfur (S_N) powders was dissolved in the mixed solution consisting of anhydrous ethylenediamine (16 mL) and absolute ethanol (16 mL) under magnetic stirring. Then, the mixed solution was transferred into a clean and dry Teflon-lined stainless-steel autoclave (50 mL). After that, the pretreated NF was placed in the autoclave with the mixed solution. Subsequently, the autoclave was heat treated in an oven for 6 h with a constant temperature of 160 °C. After cooling to r.t., the obtained Ni_3S_2@NF product was rinsed by using deionized water and ethanol several times. Finally, the rinsed Ni_3S_2@NF was dried in a vacuum oven with a constant temperature of 50 °C.

4.1.2. Preparation of $Cu(OH)_2/Ni_3S_2$ Heterostructures. Typically, 0.8 mmol of $CuSO_4{\cdot}5H_2O$ was dissolved into a hexamethylenetetramine solution with the concentration of Cu^{2+} ions being 0.125 M. Then, the as-prepared solution was transferred into a 50 mL clean and dry Teflon-lined stainless-steel autoclave, and Ni_3S_2@NF was immersed into the solution. After that, the autoclave was thermally treated in a blast dry oven for 5 h with the constant temperature maintained at 90 °C. Subsequently, the product was rinsed with the application of lots of deionized water and ethanol three times and then put into a vacuum oven for drying under 60 °C. Finally, the $Cu(OH)_2/Ni_3S_2$@NF electrode material was obtained and the loading mass of $Cu(OH)_2/Ni_3S_2$ was about 4.6 mg cm^{-2}.

4.2. Materials' Characterizations. X-ray diffraction (XRD) were analyzed on a D/Max-RA X-ray diffractometer employing Cu radiation (Kα = 1.5418 Å) with a certain scan rate (2° min^{-1}). X-ray photoelectron spectroscopy (XPS) measurements were conducted on a Thermo VG Scientific

https://doi.org/10.1021/acsomega.1c03507
ACS Omega 2021, 6, 34276−34285

KA1pha spectrometer with an Al Kα radiation and a base pressure less than 3×10^{-10} mbar. Scanning electron microscopy (SEM) images were investigated on an FE-SEM microscope (JSM-6510) with an acceleration voltage at 10 kV. Transmission electron microscopy (TEM) and high-resolution TEM (HRTEM) were observed by using a JEM-2100HR (JEOL) with an accelerating voltage of 200 kV. The measurements of N_2 adsorption−desorption isotherms of the electrodes were obtained at 77 K by using a Micromeritics ASAP2020 equipment. The specific surface areas were gained according to the Brunauer−Emmett−Teller (BET) methods, and the pore size distributions were obtained based on the Barrett−Joyner−Halenda (BJH) method.

4.3. Electrochemical Tests. Electrochemical tests of the as-prepared products were conducted on an electrochemical workstation (Metrohm Autolab 302 N). Cyclic voltammetry, galvanostatic charge−discharge, long-term cycle performance, and electrochemical impedance spectroscopy measurements were all taken out through the same workstation. A platinum (Pt) plate, an Ag/AgCl electrode, and the prepared materials (1 cm × 1 cm) played as the counter electrode, the reference electrode, and the work electrode, respectively. In addition, specific capacitances of the electrodes were calculated based on the equation $C = I\Delta t/(m\Delta V)$, in which I represents the discharge current (A), Δt denotes the time of the discharge process (s), m is the loading mass of the active materials (g), and ΔV stands for the window of the working potential (V). In the EIS measurements, the AC amplitude was kept at 5 mV and the frequency was conducted ranging from 105 to 0.1 Hz.

4.4. Symmetric Supercapacitors. To further estimate the capacitance values of the $Cu(OH)_2/Ni_3S_2$@NF electrode, an assembled supercapacitor (ASC) was fabricated as a coin-type cell by using the prepared $Cu(OH)_2/Ni_3S_2$@NF materials as electrodes together with a polyvinylidene fluoride separator in an alkaline electrolyte of the 3 M KOH solution.

■ AUTHOR INFORMATION

Corresponding Authors

Lei Xu − *Key Institute of Agricultural Facilities and Equipment, Jiangsu Academy of Agricultural Sciences; Key Laboratory for Protected Agricultural Engineering in the Middle and Lower Reaches of Yangtze River, Ministry of Agriculture and Rural Affairs, Nanjing 210014, P. R. China*; Email: xulei@jaas.ac.cn

Shaochun Tang − *Key National Laboratory of Solid State Microstructures, Department of Materials Science and Engineering, Collaborative Innovation Center of Advanced Microstructures, Jiangsu Key Laboratory of Artificial Functional Materials, College of Engineering and Applied Sciences, Nanjing University, Nanjing 210093, P. R. China; Key Haian Institute of High-Tech Research, Nanjing University, Jiangsu 226600, P. R. China*; orcid.org/0000-0003-4400-708X; Email: tangsc@nju.edu.cn

Authors

Jiansen Wang − *Key National Laboratory of Solid State Microstructures, Department of Materials Science and Engineering, Collaborative Innovation Center of Advanced Microstructures, Jiangsu Key Laboratory of Artificial Functional Materials, College of Engineering and Applied Sciences, Nanjing University, Nanjing 210093, P. R. China*

Libing Hu − *Key National Laboratory of Solid State Microstructures, Department of Materials Science and Engineering, Collaborative Innovation Center of Advanced Microstructures, Jiangsu Key Laboratory of Artificial Functional Materials, College of Engineering and Applied Sciences, Nanjing University, Nanjing 210093, P. R. China; Key Haian Institute of High-Tech Research, Nanjing University, Jiangsu 226600, P. R. China*

Xiaoya Zhou − *Key National Laboratory of Solid State Microstructures, Department of Materials Science and Engineering, Collaborative Innovation Center of Advanced Microstructures, Jiangsu Key Laboratory of Artificial Functional Materials, College of Engineering and Applied Sciences, Nanjing University, Nanjing 210093, P. R. China; Key Haian Institute of High-Tech Research, Nanjing University, Jiangsu 226600, P. R. China*

Sheng Zhang − *Key National Laboratory of Solid State Microstructures, Department of Materials Science and Engineering, Collaborative Innovation Center of Advanced Microstructures, Jiangsu Key Laboratory of Artificial Functional Materials, College of Engineering and Applied Sciences, Nanjing University, Nanjing 210093, P. R. China; Key Haian Institute of High-Tech Research, Nanjing University, Jiangsu 226600, P. R. China*

Qingshan Qiao − *Key National Laboratory of Solid State Microstructures, Department of Materials Science and Engineering, Collaborative Innovation Center of Advanced Microstructures, Jiangsu Key Laboratory of Artificial Functional Materials, College of Engineering and Applied Sciences, Nanjing University, Nanjing 210093, P. R. China; Key Haian Institute of High-Tech Research, Nanjing University, Jiangsu 226600, P. R. China*

Complete contact information is available at: https://pubs.acs.org/10.1021/acsomega.1c03507

Author Contributions

[#]J.W. and L.H. contributed equally to this work.

Notes

The authors declare no competing financial interest.

■ ACKNOWLEDGMENTS

This work was jointly supported by the Natural Science Foundation of Jiangsu Province (grant no. BK20161396), the Key Research and Development Program of Jiangsu Provincial Department of Science and Technology of China (BE2020684), and the Fundamental Research Funds for the Central Universities (14380163 and 14913411).

■ REFERENCES

(1) Pech, D.; Brunet, M.; Durou, H.; Huang, P.; Mochalin, V.; Gogotsi, Y.; Taberna, P.-L.; Simon, P. Ultrahigh-power micrometre-sized supercapacitors based on onion-like carbon. *Nat. Nanotechnol.* **2010**, *5*, 651−654.

(2) Zhong, C.; Deng, Y.; Hu, W.; Qiao, J.; Zhang, L.; Zhang, J. A review of electrolyte materials and compositions for electrochemical supercapacitors. *Chem. Soc. Rev.* **2015**, *44*, 7484−7539.

(3) Tang, S.; Zhu, B.; Shi, X.; Wu, J.; Meng, X. General controlled sulfidation toward achieving novel nanosheet-built porous square-$FeCo_2S_4$-tube arrays for high-performance asymmetric all-solid-state pseudocapacitors. *Adv. Energy Mater.* **2017**, *7*, 1601985.

(4) Ko, Y.; Kwon, M.; Bae, W. K.; Lee, B.; Lee, S. W.; Cho, J. Flexible supercapacitor electrodes based on real metal-like cellulose papers. *Nat. Commun.* **2017**, *8*, 536.

(5) Liu, C.; Yu, Z.; Neff, D.; Zhamu, A.; Jang, B. Z. Graphene-based supercapacitor with an ultrahigh energy density. *Nano Lett.* **2010**, *10*, 4863−4868.

(6) Simon, P.; Gogotsi, Y. Materials for electrochemical capacitors. *Nat. Mater.* **2008**, *7*, 845−854.
(7) Huang, P.; Lethien, C.; Pinaud, S.; Brousse, K.; Laloo, R.; Turq, V.; Respaud, M.; Demortiere, A.; Daffos, B.; Taberna, P. L.; Chaudret, B.; Gogotsi, Y.; Simon, P. On-chip and freestanding elastic carbon films for micro-supercapacitors. *Science* **2016**, *351*, 691−695.
(8) Ge, J.; Wu, J.; Fan, L.; Bao, Q.; Dong, J.; Jia, J.; Guo, Y.; Lin, J. Hydrothermal synthesis of $CoMoO_4/Co_{1-x}S$ hybrid on Ni foam for high-performance supercapacitors. *J. Energy Chem.* **2018**, *27*, 478−485.
(9) Chang, P.; Mei, H.; Zhao, Y.; Huang, W.; Zhou, S.; Cheng, L. 3D structural strengthening urchin-like $Cu(OH)_2$-based symmetric supercapacitors with adjustable capacitance. *Adv. Funct. Mater.* **2019**, *29*, 1903588.
(10) Cui, M.; Tang, S.; Ma, Y.; Shi, X.; Syed, J. A.; Meng, X. Monolayer standing MnO_2-Nanosheet covered Mn_3O_4 octahedrons anchored in 3D N-Doped graphene networks as supercapacitor electrodes with remarkable cycling stability. *J. Power Sources* **2018**, *396*, 483−490.
(11) Zhou, X.; Zhu, J.; Lu, Y.; Zhang, Y.; Hong, Y.; Wang, W.; Karimov, K.; Murtaza, I.; Wang, Q.; Dong, X. Three-dimensional Co-S-P nanoflowers as highly stable electrode materials for asymmetric supercapacitors. *ACS Sustainable Chem. Eng.* **2019**, *7*, 11448−11454.
(12) Asen, P.; Shahrokhian, S. A high performance supercapacitor based on graphene/polypyrrole/Cu_2O-$Cu(OH)_2$ ternary nanocomposite coated on nickel foam. *J. Phys. Chem. C* **2017**, *121*, 6508−6519.
(13) Zhou, X.; Qu, X.; Zhao, W.; Ren, Y.; Lu, Y.; Wang, Q.; Yang, D.; Wang, W.; Dong, X. A facile synthesis of porous bimetallic Co-Ni fluorides for high-performance asymmetric supercapacitors. *Nanoscale* **2020**, *12*, 11143−11152.
(14) Wang, L.; Liu, F.; Zhao, B.; Ning, Y.; Zhang, L.; Bradley, R.; Wu, W. Carbon nanobowls filled with MoS_2 nanosheets as electrode materials for supercapacitors. *ACS Appl. Nano Mater.* **2020**, *3*, 6448−6459.
(15) Liu, K.; Yu, C.; Guo, W.; Ni, L.; Yu, J.; Xie, Y.; Wang, Z.; Ren, Y.; Qiu, J. Recent research advances of self-discharge in supercapacitors: Mechanisms and suppressing strategies. *J. Energy Chem.* **2021**, *58*, 94−109.
(16) Vicentini, R.; Nunes, W.; Freitas, B. G. A.; Da Silva, L. M.; Soares, D. M.; Cesar, R.; Rodella, C. B.; Zanin, H. Niobium pentoxide nanoparticles @ multi-walled carbon nanotubes and activated carbon composite material as electrodes for electrochemical capacitors. *Energy Storage Mater.* **2019**, *22*, 311−322.
(17) Salanne, M.; Rotenberg, B.; Naoi, K.; Kaneko, K.; Taberna, P. L.; Grey, C. P.; Dunn, B.; Simon, P. Efficient storage mechanisms for building better supercapacitors. *Nat. Energy* **2016**, *1*, 16070.
(18) Shao, Y.; El-Kady, M. F.; Sun, J.; Li, Y.; Zhang, Q.; Zhu, M.; Wang, H.; Dunn, B.; Kaner, R. B. Design and mechanisms of asymmetric supercapacitors. *Chem. Rev.* **2018**, *118*, 9233−9280.
(19) Choudhary, N.; Li, C.; Moore, J.; Nagaiah, N.; Zhai, L.; Jung, Y.; Thomas, J. Asymmetric supercapacitor electrodes and devices. *Adv. Mater.* **2017**, *29*, 1605336.
(20) Chen, H.; Jiang, J.; Zhang, L.; Wan, H.; Qi, T.; Xia, D. Highly conductive $NiCo_2S_4$ urchin-like nanostructures for high-rate pseudocapacitors. *Nanoscale* **2013**, *5*, 8879−8883.
(21) Ray, R. S.; Sarma, B.; Jurovitzki, A. L.; Misra, M. Fabrication and characterization of titania nanotube/cobalt sulfide supercapacitor electrode in various electrolytes. *Chem. Eng. J.* **2015**, *260*, 671−683.
(22) Wang, Q.; Gao, F.; Xu, B.; Cai, F.; Zhan, F.; Gao, F.; Wang, Q. ZIF-67 derived amorphous $CoNi_2S_4$ nanocages with nanosheet arrays on the shell for a high-performance asymmetric supercapacitor. *Chem. Eng. J.* **2017**, *327*, 387−396.
(23) Huo, H.; Zhao, Y.; Xu, C. 3D Ni_3S_2 nanosheet arrays supported on Ni foam for high-performance supercapacitor and non-enzymatic glucose detection. *J. Mater. Chem. A* **2014**, *2*, 15111−15117.
(24) Chen, S.; Li, Y.; Wu, B.; Wu, Z.; Li, F.; Wu, J.; Liu, P.; Li, H. 3D meso/macroporous Ni_3S_2@Ni composite electrode for high-performance supercapacitor. *Electrochim. Acta* **2018**, *275*, 40−49.
(25) Ma, J.; Li, W.; Zhang, X.; Cheng, Y.; Zhang, F. Free-standing Ni_3S_2 nanowire derived from in-situ synthetized coordination supramolecular as electrode materials for high performance asymmetric supercapacitors. *Appl. Surf. Sci.* **2020**, *507*, 145074.
(26) Qian, H.; Wu, B.; Nie, Z.; Liu, T.; Liu, P.; He, H.; Wu, J.; Chen, Z.; Chen, S. A flexible Ni_3S_2/Ni@CC electrode for high-performance battery-like supercapacitor and efficient oxygen evolution reaction. *Chem. Eng. J.* **2021**, *420*, 127646.
(27) Dai, C.-S.; Chien, P.-Y.; Lin, J.-Y.; Chou, S.-W.; Wu, W.-K.; Li, P.-H.; Wu, K.-Y.; Lin, T.-W. Hierarchically structured Ni_3S_2/carbon nanotube composites as high performance cathode materials for asymmetric supercapacitors. *ACS Appl. Mater. Interfaces* **2013**, *5*, 12168−12174.
(28) Chou, S.-W.; Lin, J.-Y. Cathodic deposition of flaky nickel sulfide nanostructure as an electroactive material for high-performance supercapacitors. *J. Electrochem. Soc.* **2013**, *160*, D178−D182.
(29) Ji, F.; Jiang, D.; Chen, X.; Pan, X.; Kuang, L.; Zhang, Y.; Alameh, K.; Ding, B. Simple in-situ growth of layered Ni_3S_2 thin film electrode for the development of high-performance supercapacitors. *Appl. Surf. Sci.* **2017**, *399*, 432−439.
(30) Sun, M.; Li, Z.; Fang, Q.; Han, S.; Cai, C.; Li, H.; Shen, W.; Liu, X.; Fu, Y. Room-temperature synthesized porous $Cu(OH)_2$/Cu_7S_4 hybrid nanowires as a high-performance electrode material for asymmetric supercapacitors. *J. Mater. Chem. A* **2020**, *8*, 724−734.
(31) Saha, S.; Samanta, P.; Murmu, N. C.; Kuila, T. A review on the heterostructure nanomaterials for supercapacitor application. *J. Energy Storage* **2018**, *17*, 181−202.
(32) Hou, H.; Zhang, X. Rational design of 1D/2D heterostructured photocatalyst for energy and environmental applications. *Chem. Eng. J.* **2020**, *395*, 125030.
(33) Gao, Z.; Chen, C.; Chang, J.; Chen, L.; Wang, P.; Wu, D.; Xu, F.; Jiang, K. Porous Co_3S_4@Ni_3S_4 heterostructure arrays electrode with vertical electrons and ions channels for efficient hybrid supercapacitor. *Chem. Eng. J.* **2018**, *343*, 572−582.
(34) Gu, T.-H.; Kwon, N. H.; Lee, K.-G.; Jin, X.; Hwang, S.-J. 2D inorganic nanosheets as versatile building blocks for hybrid electrode materials for supercapacitor. *Coord. Chem. Rev.* **2020**, *421*, 213439.
(35) Zhang, X.; Fan, Q.; Liu, S.; Qu, N.; Yang, H.; Wang, M.; Yang, J. A facile fabrication of 1D/2D nanohybrids composed of NiCo-hydroxide nanowires and reduced graphene oxide for high-performance asymmetric supercapacitors. *Inorg. Chem. Front.* **2020**, *7*, 204−211.
(36) Dang, Z.-M.; Zheng, M.-S.; Zha, J.-W. 1D/2D carbon nanomaterial-polymer dielectric composites with high permittivity for power energy storage applications. *Small* **2016**, *12*, 1688−1701.
(37) Venkatachalam, V.; Jayavel, R. 1D/2D Co_3O_4/graphene composite electrodes for high-performance supercapacitor applications. *J. Electron. Mater.* **2020**, *49*, 3174−3181.
(38) Han, Y.; Ge, Y.; Chao, Y.; Wang, C.; Wallace, G. G. Recent progress in 2D materials for flexible supercapacitors. *J. Energy Chem.* **2018**, *27*, 57−72.
(39) Zhu, T.; Wu, H. B.; Wang, Y.; Xu, R.; Lou, X. W. D. Formation of 1D hierarchical structures composed of Ni_3S_2 nanosheets on CNTs backbone for supercapacitors and photocatalytic H_2 production. *Adv. Energy Mater.* **2012**, *2*, 1497−1502.
(40) Chao, Y.; Zheng, J.; Zhang, H.; Ma, Y.; Li, F.; Tan, Y.; Zhu, Z. Constructing film photocatalyst with abundant interfaces between CdS and Ni_3S_2 nanosheets for efficient photocatalytic hydrogen production. *Energy Technol.* **2018**, *6*, 2132−2138.
(41) Fu, W.; Zhao, Y.; Mei, J.; Wang, F.; Han, W.; Wang, F.; Xie, E. Honeycomb-like Ni_3S_2 nanosheet arrays for high-performance hybrid supercapacitors. *Electrochim. Acta* **2018**, *283*, 737−743.
(42) Ou, X.; Luo, Z. One-step synthesis of Ni_3S_2 nanoplatelets on graphene for high performance supercapacitors. *RSC Adv.* **2016**, *6*, 10280−10284.
(43) Li, C.; Zhang, D.; Cao, J.; Yu, P.; Qin, J.; Zhang, X. Ni_3S_2 Nanoparticles Anchored on d-Ti_3C_2 Nanosheets with Enhanced Sodium Storage. *ACS Appl. Energy Mater.* **2021**, *4*, 2593−2599.

https://doi.org/10.1021/acsomega.1c03507
ACS Omega 2021, 6, 34276−34285

(44) Liu, B.; Kong, D.; Huang, Z. X.; Mo, R.; Wang, Y.; Han, Z.; Cheng, C.; Yang, H. Y. Three-dimensional hierarchical $NiCo_2O_4$ nanowire@Ni_3S_2 nanosheet core/shell arrays for flexible asymmetric supercapacitors. *Nanoscale* **2016**, *8*, 10686−10694.
(45) He, D.; Wang, G.; Liu, G.; Bai, J.; Suo, H.; Zhao, C. Facile route to achieve mesoporous $Cu(OH)_2$ nanorods on copper foam for high-performance supercapacitor electrode. *J. Alloys Compd.* **2017**, *699*, 706−712.
(46) Shinde, S. K.; Dubal, D. P.; Ghodake, G. S.; Kim, D. Y.; Fulari, V. J. Nanoflower-like CuO/$Cu(OH)_2$ hybrid thin films: Synthesis and electrochemical supercapacitive properties. *J. Electroanal. Chem.* **2014**, *732*, 80−85.
(47) Zhou, S.; Feng, X.; Shi, H.; Chen, J.; Zhang, F.; Song, W. Direct growth of vertically aligned arrays of $Cu(OH)_2$ nanotubes for the electrochemical sensing of glucose. *Sens. Actuators, B* **2013**, *177*, 445−452.
(48) Zhu, D.; Yan, M.; Chen, R.; Liu, Q.; Liu, J.; Yu, J.; Zhang, H.; Zhang, M.; Liu, P.; Li, J.; Wang, J. 3D $Cu(OH)_2$ nanowires/carbon cloth for flexible supercapacitors with outstanding cycle stability. *Chem. Eng. J.* **2019**, *371*, 348−355.
(49) Chen, F.; Wang, H.; Ji, S.; Pollet, B. G.; Wang, R. Hierarchical core-shell structured $CoNi_2S_4$/Ni_3S_2@$Ni(OH)_2$ nanosheet arrays as electrode for electrochemical energy storage. *J. Alloys Compd.* **2019**, *785*, 684−691.
(50) Biesinger, M. C.; Lau, L. W. M.; Gerson, A. R.; Smart, R. S. C. Resolving surface chemical states in XPS analysis of first row transition metals, oxides and hydroxides: Sc, Ti, V, Cu and Zn. *Appl. Surf. Sci.* **2011**, *257*, 887−898.
(51) Hu, W.; Chen, R.; Xie, W.; Zou, L.; Qin, N.; Bao, D. $CoNi_2S_4$ nanosheet arrays supported on nickel foams with ultrahigh capacitance for aqueous asymmetric supercapacitor applications. *ACS Appl. Mater. Interfaces* **2014**, *6*, 19318−19326.
(52) Wang, H.; Yan, G.; Cao, X.; Liu, Y.; Zhong, Y.; Cui, L.; Liu, J. Hierarchical $Cu(OH)_2$@MnO_2 core-shell nanorods array in situ generated on three-dimensional copper foam for high-performance supercapacitors. *J. Colloid Interface Sci.* **2020**, *563*, 394−404.
(53) He, S.; Chen, W. High performance supercapacitors based on three-dimensional ultralight flexible manganese oxide nanosheets/carbon foam composites. *J. Power Sources* **2014**, *262*, 391−400.
(54) Zhao, C.; Wang, S.; Zhu, Z.; Ju, P.; Zhao, C.; Qian, X. Roe-shaped $Ni_3(PO_4)_2$/RGO/$Co_3(PO_4)_2$ (NRC) nanocomposite grown in situ on Co foam for superior supercapacitors. *J. Mater. Chem. A* **2017**, *5*, 18594−18602.
(55) Wu, J.; Shi, X.; Song, W.; Ren, H.; Tan, C.; Tang, S.; Meng, X. Hierarchically porous hexagonal microsheets constructed by well-interwoven MCo_2S_4 (M = Ni, Fe, Zn) nanotube networks via two-step anion-exchange for high- performance asymmetric supercapacitors. *Nano Energy* **2018**, *45*, 439−447.

https://doi.org/10.1021/acsomega.1c03507
ACS Omega 2021, 6, 34276−34285